J. Fluid Mech. (1997), *vol.* 350, *pp.* 149–175. Printed in the United Kingdom

Inertial Bénard–Marangoni convection

By THOMAS BOECK AND ANDRÉ THESS

Center for Physical Fluid Dynamics, Department of Mechanical Engineering,
Dresden University of Technology, 01062 Dresden, Germany

(Received 28 October 1996 and in revised form 11 June 1997)

Two-dimensional surface-tension-driven Bénard convection in a layer with a free-slip bottom is investigated in the limit of small Prandtl number using accurate numerical simulations with a pseudospectral method complemented by linear stability analysis and a perturbation method. It is found that the system attains a steady state consisting of counter-rotating convection rolls. Upon increasing the Marangoni number Ma the system experiences a transition between two typical convective regimes. The first one is the regime of weak convection characterized by only slight deviations of the isotherms from the linear conductive temperature profile. In contrast, the second regime, called inertial convection, shows significantly deformed isotherms. The transition between the two regimes becomes increasingly sharp as the Prandtl number is reduced. For sufficiently small Prandtl number the transition from weak to inertial convection proceeds via a subcritical bifurcation involving weak hysteresis. In the viscous zero-Prandtl-number limit the transition manifests itself in an unbounded growth of the flow amplitude for Marangoni numbers beyond a critical value Ma_i. For $Ma < Ma_i$ the zero-Prandtl-number equations provide a reasonable approximation for weak convection at small but finite Prandtl number. The possibility of experimental verification of inertial Bénard–Marangoni convection is briefly discussed.

1. Introduction

Experimental investigation of surface-tension-driven Bénard convection (STDBC, also called Bénard–Marangoni convection) in low-Prandtl-number fluids (liquid metals or semiconductor melts) is a difficult task, which has to date only once been accomplished successfully by Ginde, Gill & Verhoeven (1989). Numerical simulations offer the opportunity to circumvent the difficulties and high costs of experiments while imposing only a few *a priori* restrictions on the parameters of the problem. The goal of the present work is to develop direct numerical simulations of two-dimensional STDBC in low-Prandtl-number fluids extending sufficiently high into the nonlinear regime to uncover the structure of the hydrodynamic fields at increasingly high Reynolds number.

STDBC at low Prandtl number has received much less attention than at high Prandtl numbers, to which several contributions (Bestehorn 1993; Nitschke & Thess 1995; Schatz *et al.* 1995; Thess & Orszag 1995; Thess, Spirn & Jüttner 1995; Van Hook *et al.* 1995) have been made in the years since Koschmieder's (1993) survey of the subject. Numerical simulations of surface-tension-driven flows in small-Prandtl-number fluids have been performed predominantly for geometries resembling crystal growth configurations such as two-dimensional differentially heated cavities (Strani, Piva & Graziani 1983; Zebib, Homsy & Meiburg 1985; Carpenter & Homsy 1990;

Ben Hadid & Roux 1992 and references therein; Kanouff & Greif 1994) and the three-dimensional cylindrical floating-zone geometry (Levenstam & Amberg 1995). The same applies for more recent theoretical studies using stability methods, see the review article of Davis (1987). Numerical investigation of strongly nonlinear STDBC in small-Prandtl-number fluids has so far not been undertaken.

In contrast to STDBC, buoyancy-driven Rayleigh–Bénard convection (RBC) has been extensively studied numerically in the two- and three-dimensional case for both high and low Prandtl numbers. A surprising result of the numerical studies in two dimensions at small Prandtl number is the existence of inertial convection, for which the buoyancy force is balanced by the inertial terms. The flow pattern associated with this type of convection consists of rolls which act like flywheels, i.e. the amount of energy dissipated per rotation of the roll is much less than the total kinetic energy of the fluid motion. Another characteristic feature is that the heat transport (to be measured in terms of the non-dimensional Nusselt number) becomes independent of the Prandtl number. Inertial convection was apparently first observed by Veronis (1966) in two-dimensional Rayleigh–Bénard convection between free-slip boundaries and subsequently studied by Moore & Weiss (1973). It also exists in the axisymmetric geometry and in the case of no-slip boundaries as demonstrated by Jones, Moore & Weiss (1976) and Clever & Busse (1981). For STDBC an analogous regime of convection has so far not been reported. The present work is concerned with the existence of this regime in STDBC.

The paper is organized as follows. In §2 we define the mathematical model and discuss its limitations. Section 3 describes the numerical scheme used in the direct numerical simulations. Section 4 contains an account of those nonlinear flow regimes (weak convection) that are adequately described by the viscous zero-Prandtl-number model, to be defined below. In §5 we demonstrate that for sufficiently high Marangoni number Ma inertial convection is established. We also explain the asymptotic scaling laws for the dependence of the velocity and the thickness of thermal boundary layers on the Marangoni number in the limit of large Marangoni number, $Ma \to \infty$. Finally, we compare our results with RBC and outline possible extensions of this work. Details of linear stability analysis and of a perturbation scheme are given in the Appendices.

2. Formulation of the problem

2.1. *Basic assumptions*

We consider a planar fluid layer of thickness d with a free upper surface as sketched in figure 1. Our theoretical model involves the following basic assumptions: (i) zero buoyancy force, (ii) non-deflecting upper surface, (iii) two-dimensional motion, (iv) free-slip boundary conditions at the bottom.

The considerable simplification of the problem that is achieved by these assumptions is justified because STDBC in low-Prandtl-number fluids is still poorly understood.

The first assumption (i) is made to study the effects of purely thermocapillary forcing. The neglect of buoyancy is justified if the ratio of the Rayleigh to the Marangoni number Ra/Ma, measuring the relative strength of buoyancy and surface tension forces, is small. From $Ra/Ma \propto gd^2$, where g denotes the acceleration due to gravity and d is the layer thickness, it follows that buoyancy effects can be reduced by working with sufficiently shallow layers or even completely suppressed in an experiment in a microgravity environment. Under terrestrial conditions the ratio

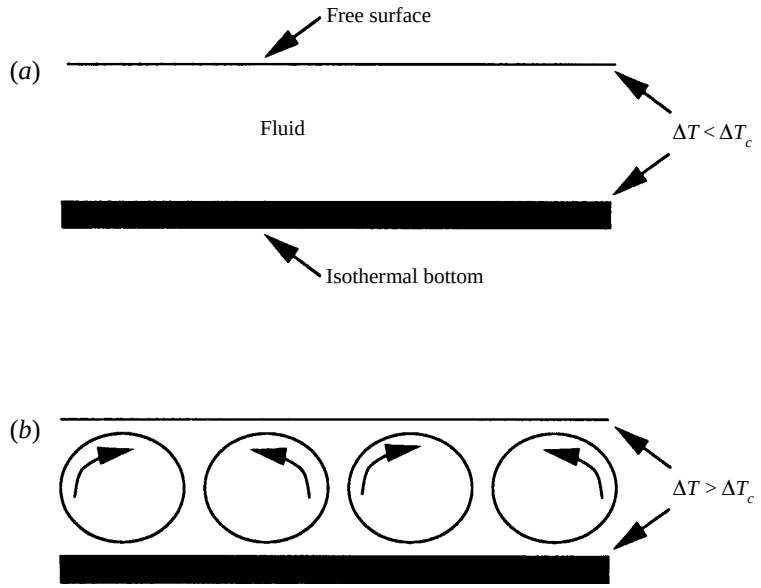

FIGURE 1. Schematic of the primary instability in surface-tension-driven Bénard convection: the thermally induced surface shear is not strong enough to overcome viscous dissipation (*a*) unless the temperature difference across the layer exceeds a finite instability threshold above which convection sets in (*b*).

Ra/Ma is approximately 0.04 for a layer of liquid tin of 1 mm depth (see Ginde *et al.* (1989) for material properties).

Assumption (ii) is adopted for reasons of conceptual simplicity and computational economy. It has already proven useful in the numerical investigation of STDBC in high-Prandtl-number fluids (Bestehorn 1993; Thess & Orszag 1995). A non-deflecting free surface inhibits vorticity generation due to free-surface curvature (Longuet-Higgins 1992; Sarpkaya 1996) and permits us to study the thermocapillary vorticity production in its pure form. Mathematically, the neglect of surface deflection is justified when the dynamic Bond number of thermocapillary convection is small, which is usually the case (Davis 1987).

The motivation to employ assumption (iii) is twofold. On the one hand, two-dimensional problems can be investigated numerically up to very high Marangoni numbers for which three-dimensional simulations are prohibitively expensive. On the other hand, quasi-two-dimensional convection in low-Prandtl-number fluids can be experimentally realized by applying a homogeneous magnetic field parallel to the free surface of the fluid. If the magnetic interaction parameter $N = \sigma_{el} B^2 l/\rho V$ (where σ_{el}, B, l, ρ, V denote electrical conductivity, magnetic field strength, lengthscale, density and characteristic velocity) is sufficiently high, the vorticity will align with the magnetic field, and the velocity field becomes quasi-two-dimensional (Moreau 1990; Davidson 1995). For a laterally unbounded system the governing hydromechanic equations decouple from the equations for the magnetic field, and the system behaves as if the magnetic field were absent. Thus, assumption (iii) is not only desirable from the computational viewpoint, but is also physically legitimate.

Our reasons for working with assumption (iv) become apparent in the light of preliminary computations performed with the no-slip boundary condition at the bottom. For this case the transition from weak to inertial convection is found to

occur only after a time-dependent (travelling wave) regime has been established, and inertial convection exhibits complex time dependence upon increasing the Marangoni number. With a free-slip bottom the generation of secondary vorticity is suppressed. The resulting behaviour is much simpler and provides the basis for an understanding of the more complex phenomena in the no-slip case.

2.2. *Governing equations*

We choose Cartesian axes with z perpendicular to the layer and all flow independent of the coordinate y. We apply periodic boundary conditions in the horizontal x-direction with periodicity length L. The fluid is assumed to be an incompressible Newtonian liquid satisfying the Navier–Stokes equation together with the continuity and heat equations. These equations read

$$\frac{\partial \boldsymbol{v}}{\partial t} + (\boldsymbol{v}\cdot\nabla)\boldsymbol{v} = -\frac{\nabla p}{\rho} + \nu\Delta\boldsymbol{v}, \tag{2.1}$$

$$\nabla\cdot\boldsymbol{v} = 0, \tag{2.2}$$

$$\frac{\partial T}{\partial t} + (\boldsymbol{v}\cdot\nabla)T = \kappa\Delta T. \tag{2.3}$$

Here $\boldsymbol{v} = v_x\boldsymbol{e}_x + v_z\boldsymbol{e}_z$ is the velocity vector, and ρ, ν and κ denote the density, kinematic viscosity and thermal diffusivity of the fluid. The surface tension acting at the free surface is assumed to be a linearly decreasing function of temperature,

$$\sigma = \sigma(T_r) - \gamma(T - T_r), \tag{2.4}$$

where T_r stands for a reference temperature.

At the isothermal, stress-free bottom at $z = 0$ the normal component of the velocity, the tangential stresses and the temperature satisfy the equations

$$v_z = 0, \qquad \frac{\partial v_x}{\partial z} = 0, \qquad T = T_b. \tag{2.5}$$

The boundary conditions at the free surface located at $z = d$ are more complicated. Because of the non-deflecting surface the kinematic boundary condition reduces to

$$v_z = 0. \tag{2.6}$$

Surface shear stresses due to surface tension gradients satisfy the equation

$$\rho\nu\frac{\partial v_x}{\partial z} = \frac{\partial \sigma}{\partial x}, \tag{2.7}$$

cf. Landau & Lifshitz (1987). With σ substituted by (2.4) this boundary condition relating surface shear to the gradient of the surface temperature is usually referred to as the Marangoni boundary condition. The thermal boundary condition is not straightforward. No rigorous derivation can be given. For STDBC the free surface cannot be isothermal for a self-sustaining convective flow as the driving stresses vanish for an isothermal free surface. Therefore, a simple phenomenological model, sometimes called Newton's law of cooling, is commonly used in this problem. It relates the heat flux across the free surface to the difference between fluid surface temperature T_s and the ambient temperature T_* by

$$-\lambda\frac{\partial T}{\partial z} = -\alpha(T_* - T_s). \tag{2.8}$$

Here λ denotes the thermal conductivity of the fluid, and α is termed the heat transfer

coefficient. In the purely conductive state ($\boldsymbol{v} = 0$) the vertical temperature profile is linear. The temperature difference across the layer is then given by

$$\Delta T_0 = T_b - T_s = \frac{Bi}{1+Bi}(T_b - T_*), \qquad Bi = \frac{\alpha d}{\lambda}, \tag{2.9}$$

with the Biót number Bi as non-dimensional parameter. It is convenient to consider the deviation θ from the the conductive profile. We therefore write

$$T = \theta + T_b - \frac{\Delta T_0}{d} z, \tag{2.10}$$

and obtain the heat equation in the form

$$\frac{\partial \theta}{\partial t} + (\boldsymbol{v} \cdot \nabla)\theta = \kappa \Delta \theta + \frac{\Delta T_0}{d} v_z. \tag{2.11}$$

The boundary conditions for the temperature perturbation θ read

$$\theta|_{z=0} = 0, \qquad \left(\lambda \frac{\partial \theta}{\partial z} + \alpha \theta\right)\Big|_{z=d} = 0. \tag{2.12}$$

Notice that $0 \leqslant \theta \leqslant T_b$ since the fluid cannot become hotter than the bottom wall.

2.3. *The small-Prandtl-number limit: viscous vs. thermal scaling*

For the non-dimensionalization of the equations, scales of length, velocity, and temperature perturbation θ are needed. A proper choice of scales allows the non-dimensional quantities to remain bounded as the Prandtl number $P = \nu/\kappa$ goes to zero. The relevant lengthscale of the problem is the layer thickness d. The appropriate timescale is d/V, where V denotes the velocity scale. We will see below that with V given, the scale of θ is determined as well. However, V is *a priori* unknown. It will turn out that two different velocity scales, namely the viscous scale $V = \nu/d$ and the thermal scale $V = \kappa/d$, are necessary to appropriately capture the dynamics of the system in the two distinct regimes to be described in §§4 and 5.

We first non-dimensionalize the equations using the viscous velocity scaling. From the Navier–Stokes equation we find $\rho\nu^2/d^2$ to be the scale for pressure, and from the heat equation it follows that $P\Delta T_0$ is the scale of θ. This scaling maintains a coupling of velocity and temperature in the limit of zero Prandtl number. The dimensionless equations and boundary conditions read

$$\frac{\partial \boldsymbol{v}}{\partial t} + (\boldsymbol{v} \cdot \nabla)\boldsymbol{v} = -\nabla p + \Delta \boldsymbol{v}, \tag{2.13}$$

$$\nabla \cdot \boldsymbol{v} = 0, \tag{2.14}$$

$$P\left\{\frac{\partial \theta}{\partial t} + (\boldsymbol{v} \cdot \nabla)\theta\right\} = \Delta\theta + v_z, \tag{2.15}$$

$$\frac{\partial v_x}{\partial z} + Ma\,\frac{\partial \theta}{\partial x} = v_z = \frac{\partial \theta}{\partial z} + Bi\,\theta = 0 \qquad \text{at } z = 1, \tag{2.16}$$

$$\frac{\partial v_x}{\partial z} = v_z = \theta = 0 \qquad \text{at } z = 0, \tag{2.17}$$

with the Marangoni number

$$Ma = \frac{\gamma \Delta T_0 d}{\rho \nu \kappa} \tag{2.18}$$

as control parameter. Assuming that all quantities remain bounded as $P \to 0$, the

left-hand side of (2.15) vanishes. This limit will be referred to as the viscous zero-Prandtl-number limit. Since the boundary conditions can still be satisfied for these equations, the viscous zero-Prandtl-number limit is spatially uniformly valid. However, the independent dynamics of the temperature field is lost because the temperature perturbation θ becomes a linear functional of v_z, i.e. θ adjusts adiabatically to the velocity field. Moreover, the conductive temperature profile is not perturbed by the convective motion of the fluid. Deviations from the conductive temperature profile arise at higher order in P.

In summary, the above equations with $P = 0$ describe convective flow at finite Reynolds number in the limit of vanishing Péclet number. We are particularly interested in the zero-Prandtl-number equations because they do not exhibit two significantly different timescales that may give rise to numerical stiffness. Another advantage consists in the saving of three Fourier transforms at each timestep in the numerical solution because the nonlinear term in the heat equation drops out.

When the thermal velocity scale applies, the scales for p and θ become $\rho\kappa^2/d^2$ and ΔT_0. In contrast to the viscous scaling, the temperature profile may change significantly due to convective motion also for small P. The equations take the non-dimensional form

$$\frac{\partial \boldsymbol{v}}{\partial t} + (\boldsymbol{v}\cdot\nabla)\boldsymbol{v} = -\nabla p + P\Delta \boldsymbol{v}, \tag{2.19}$$

$$\nabla\cdot\boldsymbol{v} = 0, \tag{2.20}$$

$$\frac{\partial \theta}{\partial t} + (\boldsymbol{v}\cdot\nabla)\theta = \Delta\theta + v_z, \tag{2.21}$$

$$\frac{\partial v_x}{\partial z} + Ma\,\frac{\partial \theta}{\partial x} = v_z = \frac{\partial \theta}{\partial z} + Bi\,\theta = 0 \qquad \text{at } z = 1, \tag{2.22}$$

$$\frac{\partial v_x}{\partial z} = v_z = \theta = 0 \qquad \text{at } z = 0. \tag{2.23}$$

By taking the zero-Prandtl-number limit in the above equations we obtain the Euler equation, i.e. the thermal zero-Prandtl-number limit describes convection at finite Péclet number in the limit of infinite Reynolds number. Since two velocity boundary conditions are in general incompatible with the Euler equation, the limit $P = 0$ cannot be spatially uniformly valid for thermal scaling. Therefore, the numerical scheme presented in §3 cannot take advantage of the thermal zero-Prandtl-number limit.

In their investigation of axisymmetric RBC, Jones *et al.* (1976) use the Péclet number Pe to distinguish weak convection (Pe small compared with unity) and strong convection (Pe not small compared with unity). We shall use these terms accordingly, i.e. convection is weak when the viscous scaling applies for $P \to 0$. Viscous and thermal units of the physical quantities are summarized in table 1. We use viscous units throughout §§3 and 4.

2.4. *Nusselt number*

The effectiveness of convective heat transport is measured by the non-dimensional Nusselt number $Nu = Q/Q_c$ defined as the ratio between the total heat flux Q and the conductive heat flux Q_c. By definition, $Nu = 1$ in the purely conductive state. Whereas for RBC between isothermal plates both Q_c and Q are uniquely defined in terms of measurable quantities, the definition of Nu for convection between non-isothermal boundaries such as STDBC or RBC with free surfaces involves some ambiguity. We shall demonstrate below that if the conventional definition of Q_c is applied, the

Quantity	Viscous unit	Thermal unit
Length	d	d
Velocity	ν/d	κ/d
Time	d^2/ν	d^2/κ
Temperature perturbation θ	$P\Delta T_0$	ΔT_0
Pressure	$\rho\nu^2/d^2$	$\rho\kappa^2/d^2$

TABLE 1. Summary of viscous and thermal units

Nusselt number will not represent an appropriate measure of the effectiveness of convective heat transport for our model of STDBC. The problem is resolved by a modified definition of Q_c. The total heat flux in STDBC can be conveniently evaluated at the free surface. Upon using (2.8), (2.9) and (2.10) we obtain

$$Q = -\lambda \int_0^L \frac{\partial T(x,d)}{\partial z} \mathrm{d}x = \frac{\lambda L \Delta T_0}{d} + \alpha L \langle \theta_s \rangle, \tag{2.24}$$

where

$$\langle \theta_s \rangle = \frac{1}{L} \int_0^L \theta(x,d) \mathrm{d}x \tag{2.25}$$

denotes the mean perturbation of the surface temperature. Using the conventional definition $Q_c = \lambda L \Delta T_0/d$ for the conductive heat flux we find

$$Nu = 1 + Bi \frac{\langle \theta_s \rangle}{\Delta T_0}. \tag{2.26}$$

Since $\langle \theta_s \rangle < \Delta T_0$ (the free surface cannot become hotter than the bottom), the Nusselt number as defined above is bounded by $1+Bi$. The reason for this unphysical behaviour is twofold. On the one hand, it reflects an intrinsic deficiency in the phenomenological boundary condition (2.8) which imposes the upper bound $\alpha(T_0 - T_*)$ on the heat flux at the free surface. On the other hand, the above definition of Q_c ignores the fact that the mean temperature difference

$$\langle \Delta T \rangle = \Delta T_0 - \langle \theta_s \rangle \tag{2.27}$$

between the bottom and the free surface is smaller in the convective state than in the conductive state in contrast to convection between isothermal boundaries where the temperature difference is prescribed. This observation suggests a modified definition of Q_c, namely to define Q_c as the total heat flux that would occur with the fluid at rest but with the free-surface temperature prescribed as in the convective state. This definition may seem impractical, but for the case of periodic boundary conditions the total conductive heat flux is uniquely determined by the mean temperature difference $\langle \Delta T \rangle$. We have

$$Q_c = \frac{\lambda L \langle \Delta T \rangle}{d}, \tag{2.28}$$

which leads to the Nusselt number

$$Nu = \frac{1 + Bi\,\langle \theta_s \rangle / \Delta T_0}{1 - \langle \theta_s \rangle / \Delta T_0}. \tag{2.29}$$

This definition correctly reflects the unlimited growth of the Nusselt number when strong convection heats the free surface up to the bottom temperature and $\langle \Delta T \rangle \to 0$. The shortcomings of the previous definition of Nu are particularly obvious for $Bi = 0$.

In the viscous zero-Prandtl-number limit Nu equals unity to leading order in P, i.e. we must proceed to higher order in P to obtain a useful result for Nu. To this end we consider the heat equation (2.15), and assume that both the velocity and the temperature perturbation are expanded in powers of P, i.e. $(\boldsymbol{v}, \theta) = \sum_{n=0}^{\infty} P^n \left(\boldsymbol{v}^{(n)}, \theta^{(n)}\right)$. Averaging the equations at order P^0 and P^1 horizontally (i.e. over planes $z = const.$) we find

$$\frac{\partial^2}{\partial z^2}\langle \theta^{(0)} \rangle = 0, \tag{2.30}$$

$$\frac{\partial^2}{\partial z^2}\langle \theta^{(1)} \rangle = \frac{\partial}{\partial t}\langle \theta^{(0)} \rangle + \frac{\partial}{\partial z}\langle v_z^{(0)} \theta^{(0)} \rangle, \tag{2.31}$$

since by continuity $\langle v_z^{(i)} \rangle = 0$ at all orders. The horizontal component in $\nabla \cdot \left(\boldsymbol{v}^{(0)} \theta^{(0)}\right)$ makes no contribution to equation (2.31). Equation (2.30) implies $\langle \theta^{(0)} \rangle = 0$. We then have

$$\frac{\mathrm{d}^2}{\mathrm{d}z^2}\langle \theta^{(1)} \rangle = \frac{\mathrm{d}}{\mathrm{d}z}\langle v_z^{(0)} \theta^{(0)} \rangle, \tag{2.32}$$

which is easily solved for $\langle \theta^{(1)} \rangle$. We find

$$\langle \theta^{(1)} \rangle\big|_{z=1} = \frac{1}{Bi + 1} \int_0^1 \langle v_z^{(0)} \theta^{(0)} \rangle \mathrm{d}z. \tag{2.33}$$

The mean surface temperature perturbation $\langle \theta_s \rangle$ (in physical units) and $Nu - 1$ become

$$\langle \theta_s \rangle = P^2 \frac{\Delta T_0}{Bi + 1} \int_0^1 \langle v_z^{(0)} \theta^{(0)} \rangle \mathrm{d}z + O(P^3), \tag{2.34}$$

$$Nu - 1 = P^2 \int_0^1 \langle v_z^{(0)} \theta^{(0)} \rangle \mathrm{d}z + O(P^3). \tag{2.35}$$

Both quantities scale as P^2 in the viscous zero-Prandtl-number limit.

3. Numerical method

The numerical procedure uses a spectral spatial discretization with Fourier series in the horizontal x-direction and a Chebyshev polynomial expansion in the vertical z-direction (Canuto *et al.* 1988; Gottlieb & Orszag 1977). Because of incompressibility, the Fourier components of v_x with non-zero wavenumber k can be computed from the Fourier components of v_z. The pressure is eliminated by taking twice the curl of the momentum equation, giving

$$\frac{\partial}{\partial t}\Delta v_z - \Delta^2 v_z = \frac{\partial}{\partial x}\left(v_z \Delta v_x - v_x \Delta v_z\right). \tag{3.1}$$

Equation (3.1) represents an evolution equation for v_z. Note that we are using the equations in the non-dimensional form obtained with viscous units. Assuming that θ is known at the free surface, all Fourier components of the velocity are determined by this equation and the boundary conditions except for the mean flow $U(z, t) = \langle v_x \rangle$.

It satisfies the equation

$$\frac{\partial U}{\partial t} - \frac{\partial^2 U}{\partial z^2} = -\frac{\partial}{\partial z}\langle v_x v_z \rangle, \tag{3.2}$$

and the boundary conditions $\partial U/\partial z = 0$ at $z = 0$ and $z = 1$ since θ is periodic. Equation (3.2) is obtained by taking the horizontal average of the x-momentum equation.

In order to derive the discrete representation we put $w = \Delta v_z$ and introduce u_k, w_k and θ_k as the Fourier components with wavenumber k of v_z, w and θ. Splitting (3.1) into two second-order equations and decomposing (3.1), (2.15), (2.16), (2.17) into Fourier modes yields the set

$$\left(\frac{\partial^2}{\partial z^2} - k^2\right) w_k - \frac{\partial w_k}{\partial t} = -\left[\frac{\partial}{\partial x}(v_z \Delta v_x - v_x \Delta v_z)\right]_k, \tag{3.3}$$

$$\left(\frac{\partial^2}{\partial z^2} - k^2\right) u_k - w_k = 0, \tag{3.4}$$

$$\left(\frac{\partial^2}{\partial z^2} - k^2\right) \theta_k + u_k - P\frac{\partial \theta_k}{\partial t} = P\,[\nabla \cdot (\boldsymbol{v}\,\theta)]_k, \tag{3.5}$$

of evolution equations for the Fourier components w_k, u_k and θ_k. The respective boundary conditions are

$$w_k = u_k = \theta_k = 0 \qquad \text{at} \quad z = 0, \tag{3.6}$$

$$w_k + Ma\,k^2 \theta_k = u_k = \frac{\partial \theta_k}{\partial z} + Bi\,\theta_k = 0 \qquad \text{at} \quad z = 1. \tag{3.7}$$

Note that the incompressibility condition has been used in deriving the boundary conditions on w, and that the mean flow equation (3.2) complements this set of equations.

For time differencing we use the implicit backward Euler scheme for the linear terms and the explicit second-order Adams–Bashforth scheme for nonlinear terms on the right-hand sides. By that, for each wavenumber, a system of three linear second-order boundary value problems is obtained. We have

$$\left(\mathrm{D}^2 - k^2 - \frac{1}{\Delta t}\right) w_k^{n+1} = \frac{w_k^n}{\Delta t} - \mathrm{AB}\left\{\left[\frac{\partial}{\partial x}(v_z \Delta v_x - v_x \Delta v_z)\right]_k\right\}^n, \tag{3.8}$$

$$\left(\mathrm{D}^2 - k^2\right) u_k^{n+1} - w_k^{n+1} = 0, \tag{3.9}$$

$$\left(\mathrm{D}^2 - k^2 - \frac{P}{\Delta t}\right) \theta_k^{n+1} + u_k^{n+1} = P\left(\frac{\theta_k^n}{\Delta t} + \mathrm{AB}\left\{[\nabla \cdot (\boldsymbol{v}\,\theta)]_k\right\}^n\right), \tag{3.10}$$

with $\mathrm{D} = \mathrm{d}/\mathrm{d}z$ and $\mathrm{AB}\{f\}^n = (3f^n - f^{n-1})/2$ from the Adams–Bashforth formula. For the mean flow, time differencing gives

$$\left(\mathrm{D}^2 - \frac{1}{\Delta t}\right) U^{n+1} = \frac{U^n}{\Delta t} - \mathrm{AB}\left\{\frac{\partial}{\partial z}\langle v_z v_x \rangle\right\}^n. \tag{3.11}$$

From (3.8)–(3.10) we see that the boundary conditions on v_z and θ can be applied directly, i.e. we can solve (3.9) and (3.10) in that order. The solution of the full system including (3.8) cannot be obtained directly in this way because the Marangoni boundary condition involves both w and θ. However, if we represent the solutions as

$$w_k = w_k^0 + \mu w_k^1 \tag{3.12}$$

$$u_k = u_k^0 + \mu u_k^1 \tag{3.13}$$

$$\theta_k = \theta_k^0 + \mu \theta_k^1, \tag{3.14}$$

then the boundary condition $w_k^0 = 0$ can be imposed at $z = 1$ and (3.8)–(3.10) can be solved one after the other for w_k^0, u_k^0 and θ_k^0. The problem for w_k^1, u_k^1 and θ_k^1 comprises (3.8)–(3.10) with zero right-hand sides and e.g. $w_k^1(z = 1) = 1$ as boundary condition. The unknown coefficient μ is then computed from the Marangoni boundary condition. In the numerical simulations the size Δt of the timestep is fixed. Hence the functions w_k^1, u_k^1 and θ_k^1 are only computed once at the start for each wavenumber k. They are stored and reused at every timestep.

In the discrete Chebyshev representation each set (3.8)–(3.10) reduces to a tridiagonal system of linear algebraic equations for the expansion coefficients. The boundary conditions are incorporated by means of the τ-method, which results in two filled rows. Nonlinear terms are computed pseudospectrally, i.e. in physical space using fast Fourier and fast Chebyshev transforms. Dealiasing is implemented by means of the 2/3-rule.

Two independent tests were performed for validation of the numerical code. The first is based on the linear stability analysis given in Appendix A. We compare the growth rate β obtained from a numerical simulation with zero nonlinear terms with the exact value from linear stability analysis. For $Ma = 70$, $P = 0.1$, $Bi = 0$, $k = 1.7003$ the simulation gives $\beta = 2.300970$, which differs by a relative error of only 3×10^{-5} from the exact value $\beta = 2.300904$ of linear stability theory (numerical parameters: $N_z = 33$ collocation points in the vertical direction, timestep 2.5×10^{-5}).

The second test is based on the perturbation solution outlined in the appendix. This solution is valid in the weakly nonlinear regime near the instability threshold, where we observe excellent agreement with direct numerical simulations. For $Bi = 0$, $k = 1.7003$ and $Ma = 58$ the kinetic energy of steady convection rolls obtained from the numerical simulation differs from the result of the perturbation procedure by a relative error of 0.33% for $P = 0$ and 0.43% for $P = 0.1$ (numerical parameters of direct simulation: $N_z = 33$ collocation points in the vertical and $N_z = 64$ points in the horizontal directions). This indicates that the computation of the nonlinear terms in the numerical code is also correct.

4. The regime of weak convection

4.1. *Primary instability and small-amplitude solutions*

We start with a linear stability analysis of the basic conductive state $\boldsymbol{v} = \theta = 0$ by repeating Pearson's (1958) computations with the no-slip boundary condition replaced by our free-slip boundary condition (2.17*a*). This straightforward analysis provides the basis for the subsequent nonlinear studies. Details are given in Appendix A. We find the neutral stability condition

$$Ma(k, Bi) = \frac{8k \sinh(k)^2 (k \cosh(k) + Bi \sinh(k))}{\cosh(k)^3 + k \sinh(k) - (2k^2 + 1)\cosh(k)}. \tag{4.1}$$

Representative neutral stability curves $Ma(k)$ for fixed values of the Biót number Bi are plotted in figure 2(*a*). The instability threshold is given by the minimum $Ma_c = Ma(k_c, Bi)$ of $Ma(k, Bi)$ with respect to k for fixed Bi. Both the critical wavenumber k_c and the critical Marangoni number Ma_c increase with increasing Biót number. In the limit $Bi \to \infty$ we find $k_c \to k_{max} \approx 2.5054$ (cf. figure 2*b*). The critical Marangoni number Ma_c as function of Bi in this limit is easily obtained

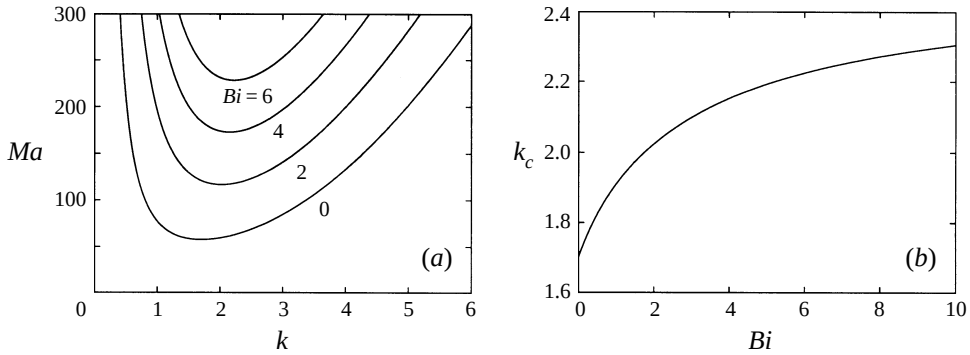

FIGURE 2. Linear stability results for a free-slip bottom: (*a*) Neutral stability curves for different Biót numbers *Bi*. The minima of these curves represent the instability threshold for given *Bi*. The neutral stability curves are independent of the Prandtl number *P*. (*b*) Wavenumber k_c at the instability threshold as function of *Bi*. In the limit $Bi \to \infty$ k_c approaches the finite value 2.5054.

by inserting k_{max} into (4.1). For any given *Bi*, both Ma_c and k_c are smaller than in the case of no-slip boundary conditions at the bottom. In particular, for $Bi = 0$ we have $Ma_c \approx 57.598$, $k_c \approx 1.7003$ to be compared with $Ma_c \approx 79.607$, $k_c \approx 1.9929$ as obtained by Pearson (1958) for the no-slip case. The higher critical Marangoni numbers in the no-slip case are due to the stabilizing effect of friction at the bottom, which is also known from RBC (Chandrasekhar 1961).

In the weakly nonlinear regime, the only feasible planform of steady two-dimensional convection consists of stationary rolls. We have obtained the amplitude and shape of the rolls in this regime by means of direct numerical simulations and of a standard perturbation method described in Appendix B. Since the perturbation method requires much less computation than direct numerical simulations, it facilitates the exploration of large ranges of Biót and Prandtl numbers in the weakly nonlinear regime. In these computations the wavenumber *k* is taken equal to the critical wavenumber $k_c(Bi)$ (cf. figure 2*b*). We have found that for $0 \leqslant Bi \leqslant 10$ with $P = 0$ and $10^{-3} \leqslant P \leqslant 10^3$ the coefficient $Ma^{(2)}$ in the expansion (B 3) (cf. Appendix B) is positive, i.e. the bifurcation to the convective state is supercritical.

The investigation of different values of *P* and *Bi* by numerical simulations is more expensive. We will therefore not consider different values of the Biót number any further. Instead, we focus on the case of prescribed heat flux ($Bi = 0$) as this case is canonical for more realistic models of heat transport across the free surface also. All of the numerical simulations reported in the remainder of the paper have been performed with $Bi = 0$ for a primitive convection cell ($L = 2\pi/k_c$, $k_c = 1.7003$) containing two counter-rotating rolls. Figure 3 shows streamfunction and vorticity plots of a single roll from direct numerical simulations with $P = 0$. The vorticity is defined by $\omega = \partial_x v_z - \partial_z v_x$. For $Ma = 57.7$ (figure 3*a*) the solution is almost identical with the neutral stability solution. Streamfunction and vorticity do not display any perceptible lateral asymmetry. The maximum of the streamfunction (corresponding to a stagnation point of the flow) is closer to the free surface than to the bottom since vorticity is generated at the free surface only. With increasing amplitude, vorticity is advected laterally and into the interior and the lateral symmetry is lost. This is accompanied by a shift of the streamfunction maximum towards the downflow region and the bottom. The effect is visible in the plots for $Ma = 60$ (figure 3*b*) but still relatively slight. It is much more pronounced in the plots for $Ma = 70$ (figure 3*c*).

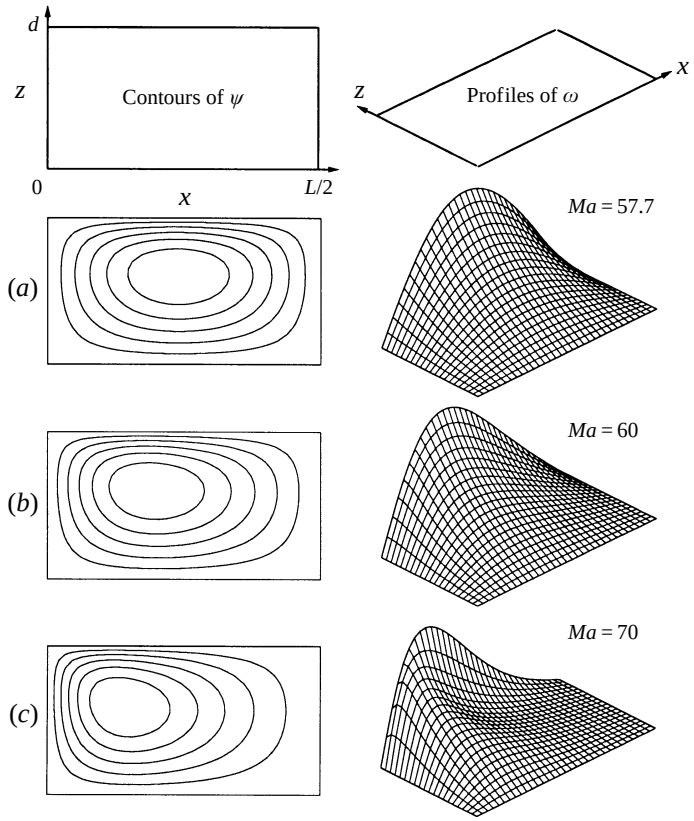

FIGURE 3. Weak convection: Streamfunction (ψ) and vorticity (ω) plots of a steady single roll for zero Prandtl number P and $Bi = 0$ as obtained from the numerical simulations. Marangoni numbers are $Ma = 58$ (a), $Ma = 60$ (b) and $Ma = 70$ (c). Spacing of the contours is equidistant. The direction of the flow is counterclockwise. Numerical resolution is $N_x = 64$, $N_z = 33$.

If the number of excited modes is small, as it is in the weakly nonlinear regime, good agreement in an integral characteristic of the flow such as the kinetic energy indicates good overall representation of the flow by the perturbation solution. On the contrary, significant differences in an integral characteristic will certainly invalidate the perturbation solution. We illustrate the limited validity of the perturbation solution for the case $P = 0$ by a comparison of the kinetic energy as obtained from the perturbation scheme and from direct numerical simulations. For a convection cell of length $L = 2\pi/k_c$ with $k_c = 1.7003$ the perturbation scheme gives

$$E = \frac{1}{2}\int_0^L \int_0^1 \boldsymbol{v}^2 \mathrm{d}x\mathrm{d}z = E_1(Ma - Ma_c) + E_2(Ma - Ma_c)^2, \tag{4.2}$$

with $Ma_c = 57.598$ and $E_1 = 6.813$, $E_2 = 0.186$. Figure 4(a) shows the energy as a function of Ma from simulations in comparison with (4.2). The perturbation solution provides an excellent approximation to the correct solution near Ma_c (cf. the test in §3), and it is still adequate at $Ma = 60$ with a relative error in the energy of 2%, but inadequate at $Ma = 70$ with an error of 35%. We attribute this to the increased asymmetry of the vorticity distributions, which cannot be well represented by the two mode perturbation ansatz (cf. figure 3 for plots of hydrodynamic fields).

After the analysis of the zero-Prandtl-number case we now wish to demonstrate

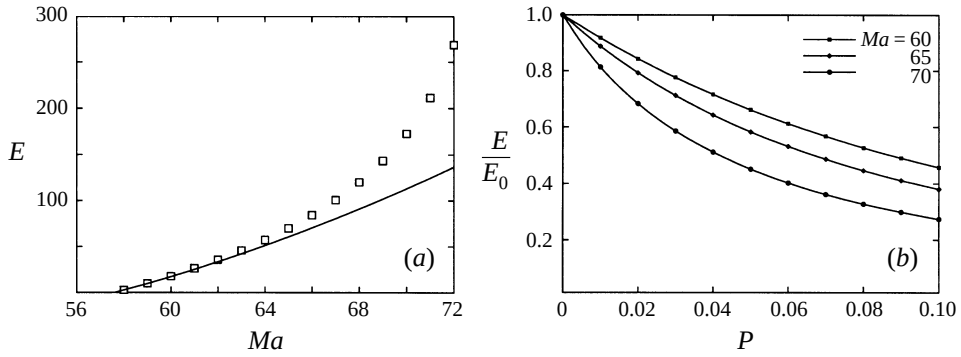

FIGURE 4. Kinetic energy of a pair of stationary rolls for weak STDBC. (*a*) Comparison of the direct numerical simulation (squares) with the result of perturbation theory (full line) for the case $P = 0$. (*b*) Results of numerical simulations for finite Prandtl number illustrating that for weak convection the zero-Prandtl-number limit is approached smoothly. However, upon increasing Ma, the $P = 0$ prediction becomes increasingly inaccurate as exemplified by the increasing slope near $P = 0$. The lines are drawn to guide the eye.

numerically that it provides a reasonable approximation for small but finite P. Figure 4(*b*) displays the kinetic energy of steady solutions at finite P normalized to the energy at $P = 0$ for different Ma. For given Ma the energy is maximal for $P = 0$ and decreases monotonically with P. This is expected, since at finite P the thermal nonlinearity can contribute to saturation. Apparently the limit $P = 0$ is approached smoothly and good agreement to within a few percent is obtained for $P \leqslant 10^{-2}$. Furthermore, figure 4(*b*) shows that the predictive power of the zero-Prandtl-number model (exemplified by the slope of $E(P)/E_0$ near $P = 0$) for fixed P deteriorates with increasing Ma. We conclude that the effect of the thermal nonlinearity will be relatively larger for the asymmetric vorticity distributions associated with increasing Ma.

4.2. *Breakdown of the viscous zero-Prandtl-number limit*

For the range of Marangoni numbers explored so far, the zero-Prandtl-number equations can be used to obtain approximate steady solutions valid for small but finite P. This useful property breaks down in a dramatic way when Ma becomes larger than $Ma_i \approx 73.4$. In numerical simulations of the zero-Prandtl-number equations we then observe a catastrophic exponential growth of the kinetic energy with no tendency to nonlinear saturation, which finally leads to a blow-up of the numerical code. We have checked by performing simulations with different initial conditions and spatial resolutions that this energy catastrophe is a robust feature of the zero-Prandtl-number model of two-dimensional STDBC. We illustrate this surprising fact with a simulation performed at $Ma = 80$. The steady solution corresponding to $P = 0.1$ is chosen as initial condition, and the Prandtl number is put equal to zero at $t = 0$. Figure 5 shows snapshots of the temporal evolution of streamfunction and vorticity fields. At $t = 0.25$ (figure 5*a*) streamfunction and vorticity look similar to the plots for $Ma = 70$ shown in figure 3. As time increases, vorticity is carried further away from the free surface with the flow. The plots for $t = 1.25$ (figure 5*b*) display the buildup of vorticity around the perimeter of the roll, whose streamfunction accordingly becomes more symmetrical. The process continues and leads to an almost constant vorticity distribution in the interior of the roll, as can be seen from the vorticity plot for $t = 2.25$ (figure 5*c*). In the course of the further evolution, the interior region of constant vorticity enlarges,

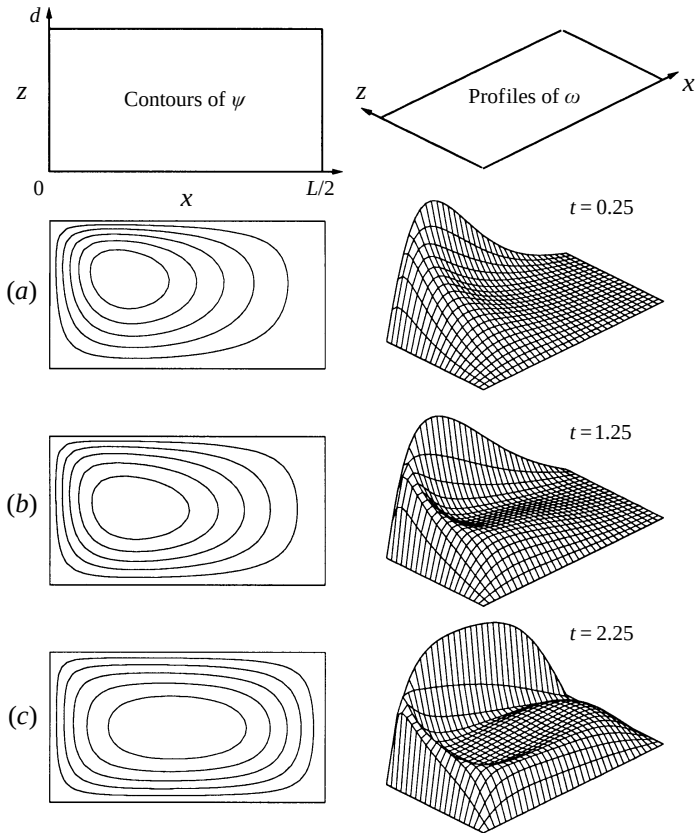

FIGURE 5. Energy catastrophe at zero Prandtl number: temporal evolution of streamfunction and vorticity in a simulation with $P = 0$ at $Ma = 80$. Snapshots taken at time $t = 0.25$ (a), $t = 1.25$ (b) and $t = 2.25$ (c). The total kinetic energy in (c) is by more than two orders of magnitude higher than in (a). Numerical resolution is $N_x = 128$, $N_z = 65$.

which causes steeper flanks along the perimeter of the constant region. Apart from that, the shape of the vorticity profile remains essentially the same.

The temporal evolution of the kinetic energy in this run is displayed in figure 6. We observe an exponential growth in the energy up to values of 10^7 with no indication of saturation. This behaviour can be explained on the basis of the observation of constant vorticity together with the high symmetry of the streamfunction. For an almost constant vorticity distribution the Navier–Stokes nonlinearity becomes effectively irrotational. Since it is then balanced by pressure gradients, it ceases to provide a means of nonlinear saturation. In the zero-Prandtl-number equations, the driving shear stress at the free surface represents a linear functional of the velocity field and will therefore grow without bound with the velocity of the interior motion. Without the contribution of the nonlinear term, only linear forcing and dissipation terms act in the equations. For sufficiently high Marangoni number the forcing will exceed viscous dissipation, and an exponential growth of the flow amplitude with time occurs.

Although none of our simulations of the zero-Prandtl-number equations for $Ma > Ma_i$ exhibits a tendency to nonlinear saturation, we cannot completely rule out the possibility of saturation by a further reorganization of the vorticity distribution.

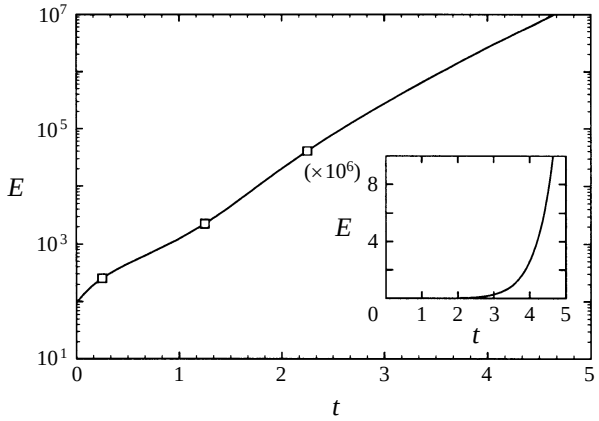

FIGURE 6. Temporal evolution of the kinetic energy E in the simulation shown in figure 5. E is given in viscous units for a single pair of rolls. Square symbols indicate the times at which snapshots for figure 5 were taken. Inset shows a linear plot of the energy.

A mathematically rigorous proof of unlimited energetic growth for $t \to \infty$ would require an estimate showing that $\mathrm{d}E/\mathrm{d}t$ has a positive lower bound for any admissible hydrodynamic field. Unfortunately, we were not able to derive such a bound by energy stability methods (Straughan 1992). While it appears unlikely that nonlinear saturation is possible for a laminar flow, the system might well evolve into a state of two-dimensional turbulence that is out of reach for our present computational capabilities. Figure 5(*a*) shows the development of a vortex sheet below the free surface. For sufficiently high Reynolds number vortex sheets are prone to Kelvin–Helmholtz instability which can lead to turbulence. Since the Reynolds number increases exponentially with time, it is clear that the flow displayed in figure 5(*c*) may become unstable at late times, leading to a complex spatio–temporal behaviour. The resulting turbulent state could dissipate kinetic energy more efficiently than the laminar boundary-layer flow due to the enstrophy cascade to high wavenumbers (Frisch 1995). Detection of this hypothetical state would require either direct numerical simulations at much higher spatial resolution or a linear stability analysis of the growing solution, both beyond the scope of the present work.

Finally, it is interesting to note that the growth of the energy is not affected by the circumstance that the curl of the nonlinear term does *not* exactly vanish in contrast to RBC between free-slip plates as noted by Jones *et al.* (1976). This shows that the energy catastrophe is an intrinsic feature of two-dimensional zero-Prandtl-number convection, independent of the specific forcing mechanism.

5. The regime of inertial convection

5.1. *Transition to strong convection*

The unbounded growth of the flow amplitude no longer takes place if the numerical simulations are performed for finite values of the Prandtl number. This can be attributed to the action of the thermal nonlinearity in equation (2.15). Steady solutions are also attained for $Ma > Ma_i$. For small P we observe the almost constant vorticity distributions in the interior of the individual rolls that were described in the previous section. Because of the thermal mechanism of nonlinear saturation, physical quantities are of similar magnitude on the thermal scale. This scaling is characteristic of strong

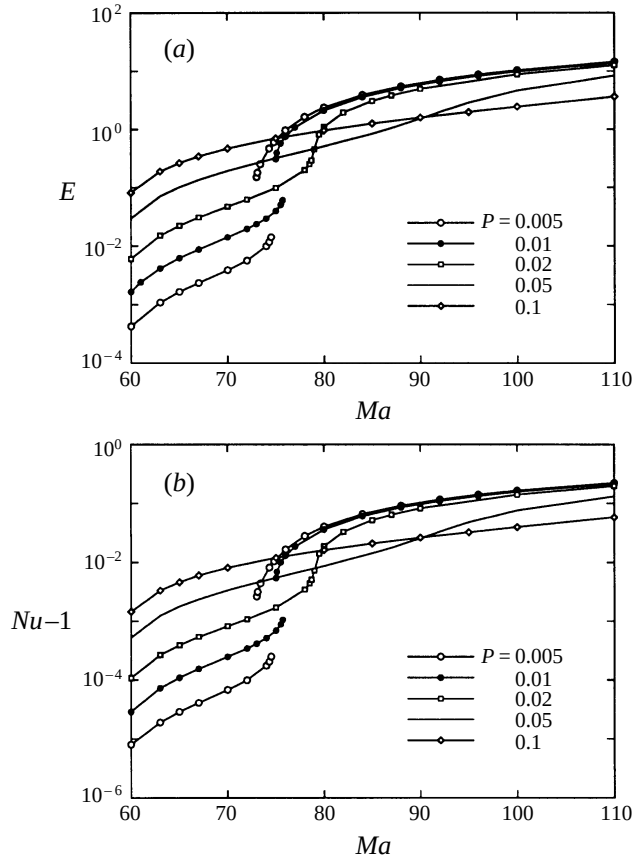

FIGURE 7. (*a*) Kinetic energy E of a single pair of rolls in thermal units as function of Ma. Transition to inertial convection is discontinuous for sufficiently small P. In the range of validity of the viscous zero-Prandtl-number limit the energy scales with P^2. (*b*) Nusselt number as function of Ma. As for the kinetic energy, $Nu - 1$ scales with P^2 for $Ma < Ma_i$, where the viscous zero-Prandtl-number limit is valid. Spatial resolution in the inertial regime is $N_x = 64$, $N_z = 65$ for $P > 0.01$, and $N_x = 128$, $N_z = 65$ for $P \leqslant 0.01$.

convection. We shall call this regime inertial convection in analogy to RBC, since the flows exhibit the flywheel property described in the Introduction. Notice that we use thermal units from now on for the rest of this section.

The transition from weak to inertial convection occurs in a narrow interval of Marangoni numbers and leads to significantly different flow fields. This can also be inferred from the integral quantities plotted in figure 7, where the kinetic energy of a single convection cell and the Nusselt number are shown as function of Ma for different values of P. The replacement of the viscous by the thermal scaling is evident from the almost identical curves of $Nu(Ma)$ for $P = 0.01$ and $P = 0.005$ for $Ma > 80$. Moreover, the transition to the inertial regime is discontinuous for these small Prandtl numbers. The subcritical bifurcation associated with the discontinuous transition is shown schematically in figure 8. For a given Prandtl number P we define $Ma_w(P)$ as the minimum value of Ma for the inertial branch and $Ma_i(P)$ as maximum value of Ma for the weak solution branch. Table 2 lists Ma_i and Ma_w for several Prandtl numbers. Notice that both Ma_i and Ma_w are shifted towards higher values as P increases.

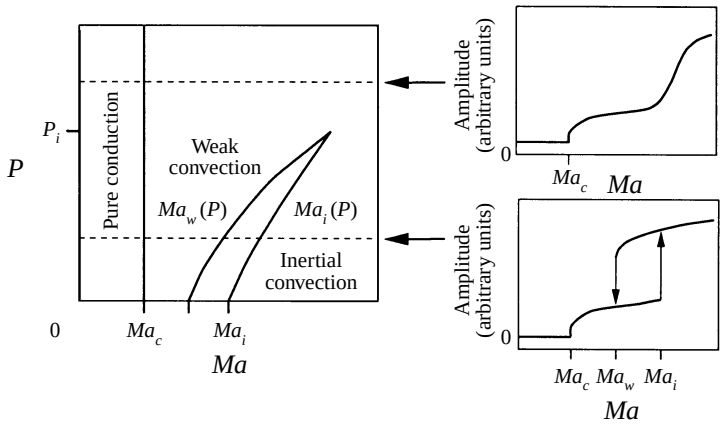

FIGURE 8. Schematic bifurcation diagram. The transition to inertial convection proceeds via a subcritical bifurcation for $P < P_i$. Inertial and weak convection coexist in the interior of the region bounded by the curves $Ma_w(P)$ and $Ma_i(P)$. See table 2 for values of Ma_w and Ma_i for four different Prandtl numbers.

P	Ma_w	Ma_i
0	71.3	73.4
0.0025	72.1	74.0
0.005	73.0	74.5
0.01	75.1	75.7

TABLE 2. Estimates for Ma_w and Ma_i from numerical simulations in a primitive convection cell with periodicity length as at onset of convection. The figures represent upper bounds for Ma_w and lower bounds for Ma_i with an accuracy of 0.1.

The bifurcation is of hydrodynamical origin since even for $P = 0$ an inertial branch of steady solutions exists in addition to the weak branch from $Ma_w(0) \approx 71.3$ on. For these flows constant-vorticity regions begin to form due to spreading of surface-generated vorticity around the roll perimeter, but viscous dissipation is still sufficient to prevent unbounded exponential growth. However, the kinetic energy associated with the inertial solutions at $P = 0$ increases dramatically (by two orders of magnitude) over the narrow interval $71.3 < Ma < 73.3$ of Marangoni numbers. Because of the high cost of these computations due to slow convergence and high resolution requirements we stopped tracing this branch at $Ma = 73.3$. It may or may not continue beyond the inertial threshold Ma_i. At finite P advection of temperature contributes to nonlinear saturation, i.e. for fixed Ma the flow amplitude is reduced. This accounts for the monotonic growth of Ma_w and Ma_i with P. Moreover, increasing P reduces the saturation energies on the inertial branch, i.e. it leads to smaller Reynolds numbers. Thus, by increasing P the branches can eventually join smoothly. The subcritical bifurcation vanishes at a Prandtl number P_i in the interval $0.01 < P_i < 0.02$. We can formally distinguish weak and inertial convection only for Prandtl numbers below P_i. As a final observation we note that for inertial convection both kinetic energy and Nusselt number increase as P is reduced as can be seen in figure 7. The surprising effect that heat transport becomes more efficient by reducing P exists also in RBC in two dimensions between free-slip boundaries (Moore & Weiss 1973).

In inertial convection, the vorticity is effectively constant in the interior of the

individual rolls with boundary layers to match the boundary conditions. For small P, these boundary layers are very thin, and the properties of the flow in the interior become independent of P. In the numerical simulations, the vorticity boundary layers determine the spatial resolution requirements. Resolution must be increased when P is reduced. For high Marangoni numbers our simulations of a single convection cell ($L = 2\pi/k_c$) were therefore restricted to the moderately small Prandtl numbers 0.02, 0.05 and 0.1. The highest Marangoni number was reached for $P = 0.1$. We have ensured sufficient resolution by inspection of the vorticity field. Because Chebyshev polynomials provide a very fine spacing of collocation points near the vertical boundaries, insufficient resolution will mostly arise in the horizonal direction. Resolution was increased when small-scale oscillations due to insufficiently resolved boundary layers showed up in horizontal cuts through the layer taken at serveral values of z. We have also checked that the vorticity has the same sign throughout the entire domain occupied by an individual roll.

Figure 9 presents a series of temperature and vorticity plots for $P = 0.1$ at different Ma. We have also plotted the horizontally averaged fields to highlight boundary layer formation. The first plots show weak convection at $Ma = 60$ (figure 9*a*) with an almost unperturbed temperature distribution. For $Ma = 150$ (figure 9*b*) the mean temperature profile still appears linear, but the total temperature difference across the layer is already significantly reduced. The isotherms are no longer parallel, but are compressed near the bottom in the downflow region and near the free surface in the upflow region, indicating a significant convective heat transport. Due to the relatively large P the vorticity profile has not yet developed the pronounced constant region that is present in all plots for higher Ma. With increasing Marangoni number the rotation of the roll speeds up further. Correspondingly, the mean temperature profile becomes flatter and the temperature difference across the layer decreases. At $Ma = 600$ (figure 9*c*) the isotherms are almost vertical in the interior of the roll, and the spacing is relatively high. From the plots for $Ma = 2400$ and $Ma = 9600$ (figures 9*d* and 9*e*) we see that the isotherms are increasingly displaced from the interior of the roll, i.e. with increasing Ma the roll develops an isothermal core and thermal boundary layers. This is also observed in the mean temperature profiles. Note that the slope of the mean temperature is always the same both at the free surface and the bottom because of the prescribed heat flux.

5.2. *Asymptotic behaviour at large Marangoni number*

The numerical simulations also demonstrate the existence of steady convection rolls at large values of the Marangoni number. Figures 10 and 11 show that in the limit $Ma \to \infty$ simple scaling behaviour with Ma applies for the hydrodynamic fields, which can be attributed to the boundary layer character of the temperature field (cf. figure 9*d*, *e*).

The boundary layer structure of both the temperature and vorticity field suggests the use of asymptotic methods to obtain approximate solutions and to derive the scaling relations from first principles. However, because of the non-trivial geometry and boundary conditions an asymptotic solution valid in the entire spatial domain cannot be obtained by simple means. We shall present a simple model that does not take into account the detailed spatial structure of the flow, but nevertheless predicts scaling exponents in agreement with the numerical simulations. We also note that similar scaling laws have been found previously in a boundary layer analysis of interfacial mass transfer in the presence of convection driven by the concentration–capillary effect (Ruckenstein 1968; Slin'ko, Dil'man & Rabinovich 1983).

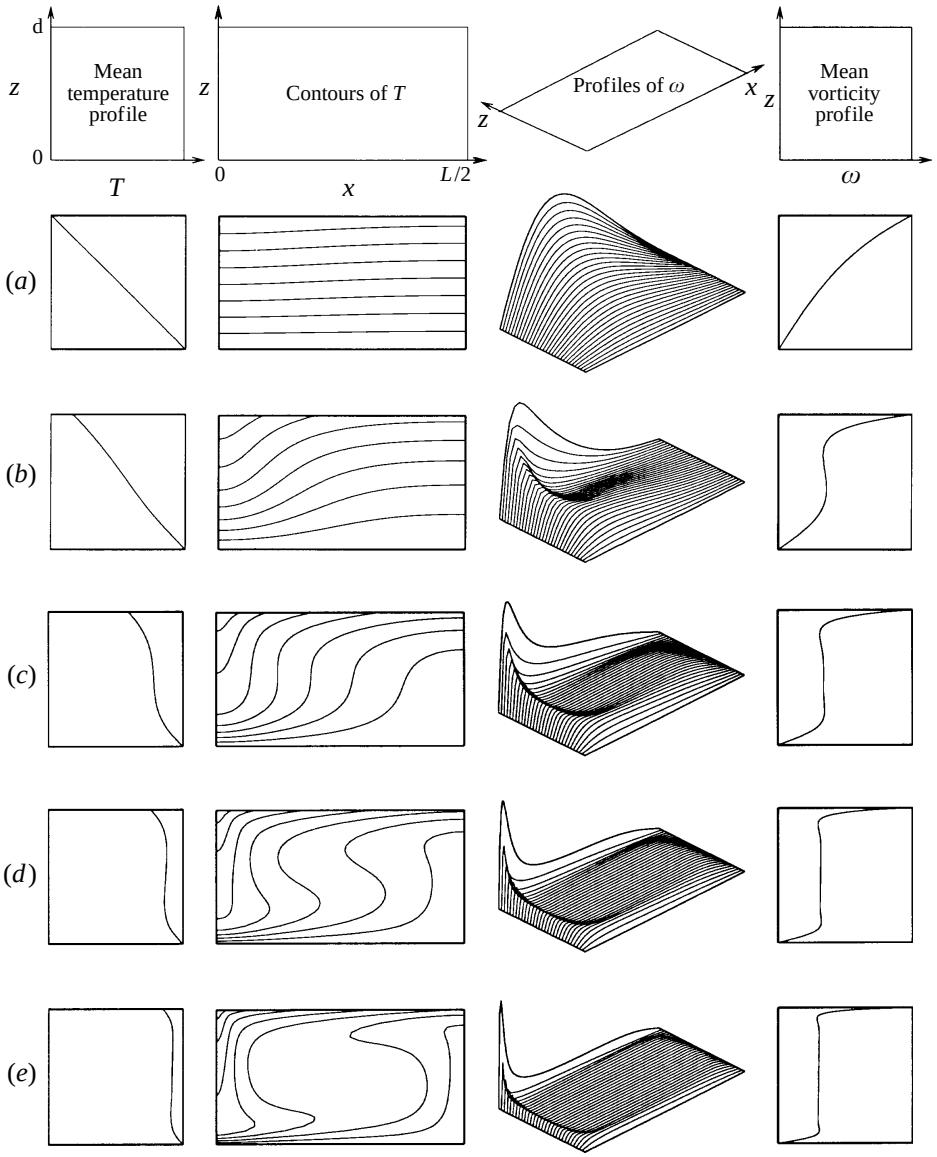

FIGURE 9. Inertial convection: temperature and vorticity plots of a steady single roll ($P = 0.1$). Marangoni numbers are $Ma = 60$ (*a*), $Ma = 150$ (*b*), $Ma = 600$ (*c*), $Ma = 2400$ (*d*) and $Ma = 9600$ (*e*). Spacing of contours is equidistant. Axes for the mean vorticity profiles are normalized to maximum values. In all cases, the streamfunction looks similar to figure 5(*c*). Note the formation of thermal boundary layers upon increasing *Ma*. Parameters are given in table 3.

The model is derived in two steps. First, we ignore the detailed structure of the velocity field and estimate the difference ΔT_h in surface temperature across a single roll on the basis of a boundary layer approximation to the heat equation. This provides a relation between ΔT_h, which generates the driving shear stress at the free surface, and the characteristic velocity V in the thermal boundary layer. The second step takes the mechanical problem into account in order to close the model and to bring in the Marangoni number. We close the model with the help of the energy budget

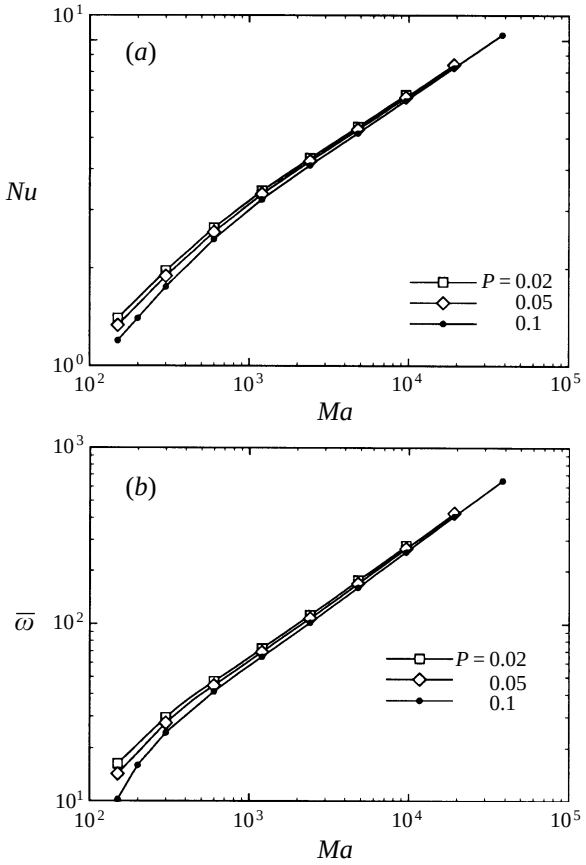

FIGURE 10. Asymptotic behaviour of inertial convection: power–law scaling with Ma of the Nusselt number (a) and the average of the vorticity over the volume of an individual roll (b). Scaling exponents are 1/3 for (a) and 2/3 for (b) in agreement with the boundary layer model of §5.2.

in the steady state, where thermocapillary energy production and viscous dissipation balance.

In the first step we consider a roll with isothermal core and thermal boundary layers at the free surface and the bottom and suppose that the velocity in the core and in the boundary layers is of the same order V. The boundary layer approximation to the equation for the temperature in both layers reads

$$v_x \frac{\partial T}{\partial x} = \frac{\partial^2 T}{\partial z^2}, \tag{5.1}$$

giving the boundary layer thickness $\delta \propto V^{-1/2}$ since the width L of the roll is $O(1)$. From the prescribed heat flux $\partial T/\partial z = -1$ at the top it follows that the temperature difference across the free-surface layer is of order δ. In the steady state, the same integral heat flux must be present at the bottom, hence the temperature difference across the thermal boundary layer at the bottom is the same as for the free-surface layer. The mean temperature difference $\langle \Delta T \rangle$ between bottom and free surface will therefore also be of order δ. For ΔT_h we assume that it is of the same order as the total temperature difference across the layer, i.e. it is $O(\delta)$, too.

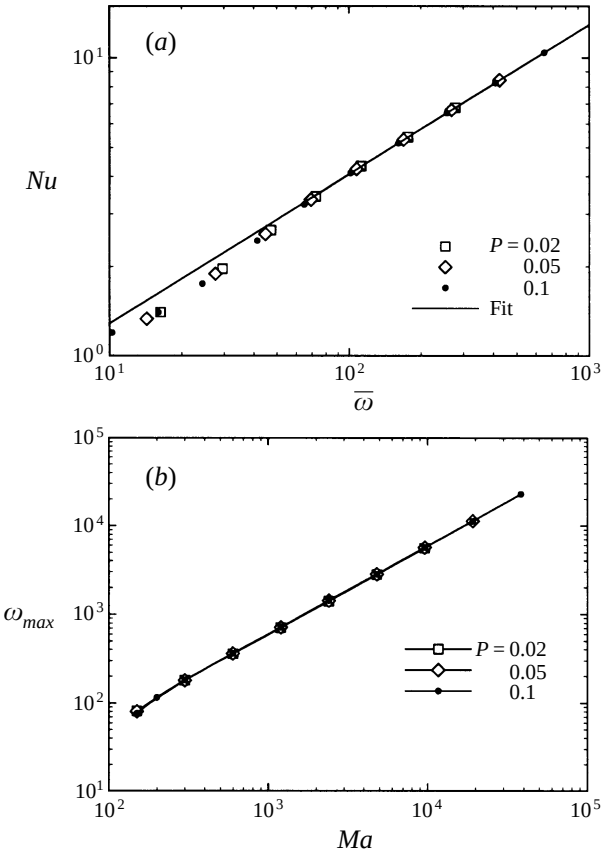

FIGURE 11. (*a*) The thermal boundary layer scaling relation $\delta \propto V^{-1/2}$ is verified by plotting the Nusselt number ($\propto \delta^{-1}$) as function of the volume average of the vorticity ($\propto V$). The straight line corresponds to $Nu \propto \omega^{1/2}$. (*b*) The maximum value of the vorticity ω_{max} attained at the free surface is proportional to Ma.

Let us now consider the balance of energy input and dissipation. Starting from the Navier–Stokes equation, the energy budget is obtained by multiplication with $\boldsymbol{v}$ and integration over the volume of the roll. For a steady state we have

$$-\int_0^L v_x \omega|_{z=1}\,\mathrm{d}x = \int_0^L \int_0^1 \omega^2 \mathrm{d}z\mathrm{d}x, \tag{5.2}$$

since $\omega = \partial_x v_z - \partial_z v_x$ vanishes on all other boundaries. On the left-hand side ω is estimated from the Marangoni boundary condition (2.22) with the temperature gradient ΔT_h. The velocity is of order V, which was already used above. For the right-hand side we assume that the bulk gives the major contribution to the integral. Because of the flywheel property, vorticity and velocity are of the same order in the core, hence ω is of order V on the right-hand side in equation (5.2). With these estimates of order it follows from (5.2) that

$$MaV\Delta T_h \propto V^2. \tag{5.3}$$

Using $\Delta T_h \propto \delta \propto V^{-1/2}$, $\langle \Delta T \rangle \propto \delta$ and the definition (2.29) we obtain

$$V \propto Ma^{2/3}, \quad \Delta T_h \propto Ma^{-1/3}, \quad \delta \propto Ma^{-1/3}, \quad Nu \propto Ma^{1/3}. \tag{5.4}$$

Ma	N_x	N_z	Nu	$\bar{\omega}$	E	$\omega_{\max}$
1200	256	65	3.24	65.1	450	716
2400	512	65	4.12	102	1080	1430
4800	512	65	5.18	161	2660	2830
9600	512	65	6.54	256	6710	5670
19200	1024	129	8.26	408	17000	11300
38400	1024	129	10.42	650	43000	22700
Computed exponent			0.336	0.671	1.34	1.00
Predicted exponent			1/3	2/3	4/3	1

TABLE 3. Numerical data from simulations with $P = 0.1$. N_x and N_z denote the number of collocation points in x and z. E stands for the kinetic energy of a single convection cell consisting of a pair of counter-rotating rolls. See text for meaning of other symbols. The scaling exponents have been computed using the data from $Ma = 4800$ on.

The scaling relations are in good agreement with our numerical data. Figure 10 shows the Nusselt number and the volume average of the vorticity $\bar{\omega}$ as function of Ma. Good power-law scaling applies for about one decade of Marangoni numbers for $P = 0.1$. Scaling exponents computed from the data deviate by only about 1% from the predicted values (cf. table 3 for the data from the simulations and further scaling exponents for other quantities). Particularly good agreement with the scaling exponent from the data only about 0.2% in error is obtained for the relation between Nu and $\bar{\omega}$ plotted in figure 11(a).

As mentioned before, we have not attempted to model corner regions. Nevertheless, a prominent feature of the vorticity field visible in figure 9(e) is a corner effect, namely the peak at the free surface in the downflow region. Let us briefly discuss the origin of this peak and its effect on the validity of our model. It can be expected that the peak results from the breakdown of the boundary layer approximation for T in the corner. We have confirmed this by numerical simulations with prescribed streamfunction when the temperature acts as a passive scalar. In these simulations constant vorticity was prescribed in the interior of the cell with thin layers to satisfy $\omega = 0$ on all boundaries. The structure of the temperature field is fairly similar to simulations of the full Marangoni problem at sufficiently small P. On the free surface $\partial T/\partial x$ has a maximum of order 1 at a distance of order δ from the stagnation point. The Marangoni boundary condition turns this into the vorticity peak with a height of order Ma present in the simulations of the full problem. Simple arguments show that the contributions from this peak are not dominant in the integrals on either side in equation (5.2), but they appear to be of the same order as the terms considered in deriving the scaling relation. Figure 11(b) shows the scaling of the maximum vorticity with Ma.

6. Discussion and conclusions

With the numerical simulations reported in the previous sections we have explored a large range of Marangoni numbers. We feel that we have analysed most of the essential physical phenomena contained in our two-dimensional model of STDBC at small Prandtl number. The major result of this work consists in the demonstration that inertial convection is not only a feature of RBC but also of purely STDBC.

In our model of STDBC, a second critical Marangoni number must be exceeded for inertial convection to occur. This is not the case in two-dimensional free-slip RBC. In

this system, the nonlinear term in the Navier–Stokes equation is already irrotational for the neutral stability mode, and the regime of weak convection is not present. However, this is not typical of inertial RBC. For no-slip boundary conditions there is also a regime of weak convection, and inertial convection occurs only for Rayleigh numbers beyond a critical value Ra_i that is larger than the instability threshold. Busse & Clever (1981) have computed an analytical estimate for Ra_i, which is about four times larger than the threshold Ra_c of convection. This is in reasonable agreement with numerical findings (Clever & Busse 1981). For the axisymmetric geometry, Jones *et. al.* (1976) have also found $Ra_i > Ra_c$ with free-slip top and bottom boundaries. In the two-dimensional free-slip case STDBC and RBC both exhibit increasing strength of the convective heat transport with $P \rightarrow 0$ in the inertial regime. This is in contrast to the other cases of RBC, where increasing P always gives higher Nusselt number. However, a subcritical bifurcation to inertial convection as in our model of STDBC is not known from any of the systems displaying inertial RBC.

In contrast to the critical parameters for the onset of convection, which are obtained from a linear analysis, the computation of the inertial Rayleigh/Marangoni number in the limit $P \rightarrow 0$ is a nonlinear problem. Jones *et. al.* (1976) have formulated this problem for their axisymmetric model of RBC. It was solved analytically by Proctor (1977) for a different model of RBC with suitably simplified geometry, namely a cylinder with a no-slip perimeter on which the temperature is prescribed. The inertial Rayleigh number Ra_i of this model problem is in reasonable agreement with the analytical approximation of Busse & Clever (1981) for the layer with no-slip boundaries. A model problem for STDBC in the same spirit as Proctor's for RBC could provide very valuable additional insight besides another estimate of Ma_i because it reflects the transition to inertial convection more clearly. However, the formulation of such a model problem appears to be not straightforward.

Inertial convection seems to be theoretically well established and understood, but experimental support is apparently still lacking even for Rayleigh–Bénard systems. In STDBC there is only the investigation by Ginde *et al.* (1989) to date. In contrast to the onset of convection, transition to inertial STDBC will be accompanied by virtually discontinuous changes in flow quantities such as the velocity amplitude. These changes should be no more difficult to detect than the onset of convection itself. Figure 12 displays our prediction of the onset of inertial convection in a hypothetical two-dimensional experiment performed with the same parameters as the Ginde *et al.* (1989) liquid-tin experiment. We have plotted an integral velocity based on the kinetic energy, which should be typical of the average surface velocity, as function of the applied temperature difference based on our numerical data for $P = 0.02$ (cf. figure 7*a*). Buoyancy effects have been neglected.

However, the lack of experimental evidence for inertial convection in low-Prandtl-number fluids is not merely attributable to the difficulties of handling such fluids, but probably also to three-dimensionality. In RBC rolls become unstable to time-dependent three-dimensional perturbations for only slightly supercritial Rayleigh number (Clever & Busse 1974). We expect that this is also the case in STDBC. The importance of two-dimensionality for inertial convection is reinforced by numerical studies in three dimensions. According to Clever & Busse (1990) and Thual (1992) the viscous zero-Prandtl-number limit does not break down, but gives results representative for small P over the entire range of parameters studied by these authors. However, these studies do not rule out the existence of a three-dimensional form of inertial convection, which remains an unresolved problem, in particular for STDBC.

Within the two-dimensional model of STDBC the free-surface heat transport needs

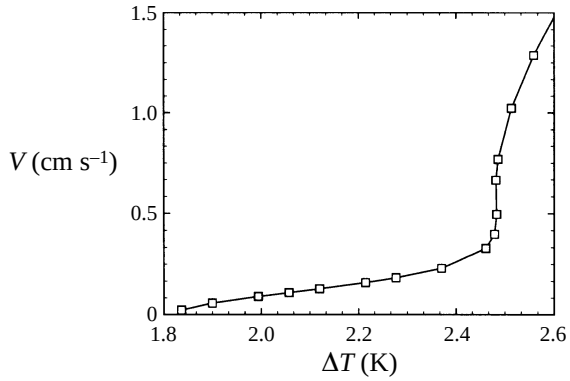

FIGURE 12. Typical average surface velocity in a layer of liquid tin ($d = 0.58$ cm) as function of the applied temperature difference as predicted from our numerical results for $P = 0.02$. Buoyancy has been neglected.

further investigation. As discussed in §2.4, the present thermal boundary condition is unsatisfactory. The derivation of a more realistic boundary condition rests on the equations of the two-layer system on which STDBC is actually based. These questions have already been addressed by Nitschke, Bestehorn & Thess (1996) in the context of high-Prandtl-number STDBC. Systematic investigation of the model with a no-slip bottom is also outstanding, with interesting time-dependent phenomena expected to occur.

We are grateful to Christian Karcher and the referees for useful comments. This work is supported by the Deutsche Forschungsgemeinschaft under grants Th 497/9-1 and Th 497/9-2.

Appendix A. Primary instability

Based on the viscous scaling (equations (2.13)–(2.17)), the normal-mode equations and boundary conditions (cf. Pearson 1958; Chandrasekhar 1961) read

$$\left(\mathrm{D}^2 - k^2 - \beta\right)\left(\mathrm{D}^2 - k^2\right) f(z) = 0, \tag{A 1}$$

$$\left(\mathrm{D}^2 - k^2 - P\beta\right) g(z) + f(z) = 0, \tag{A 2}$$

$$\mathrm{D}^2 f(1) + Ma\, k^2 g(1) = 0, \tag{A 3}$$

$$\mathrm{D}^2 f(0) = f(0) = g(0) = 0, \tag{A 4}$$

$$f(1) = \mathrm{D}g(1) + Bi\, g(1) = 0, \tag{A 5}$$

where $\mathrm{D} = \mathrm{d}/\mathrm{d}z$ and the functions $f(z)$ and $g(z)$ are defined by

$$v_z(x, z, t) = f(z)\mathrm{e}^{\mathrm{i}kx+\beta t}, \qquad \theta(x, z, t) = g(z)\mathrm{e}^{\mathrm{i}kx+\beta t}. \tag{A 6}$$

With $\beta \neq 0$, $f(z)$ and $g(z)$ take the form

$$f(z) = \sinh(kz) - \frac{\sinh\left((k^2+\beta)^{1/2}z\right)\sinh(k)}{\sinh\left((k^2+\beta)^{1/2}\right)}, \tag{A 7}$$

$$g(z) = \frac{\sinh(kz)}{P\beta} - \frac{\sinh\left((k^2+\beta)^{1/2}z\right)\sinh(k)}{(P-1)\beta\sinh(k^2+\beta)^{1/2}} + G\sinh\left((k^2+P\beta)^{1/2}z\right). \tag{A 8}$$

The coefficient G must be chosen such that the thermal boundary condition at the free surface is satisfied. The growth rate β is determined by the Marangoni boundary condition (A 3), which gives an implicit analytical expression $Ma(k, \beta, Bi, P)$ for β.

For neutral stability ($\beta = 0$), the analytical solution for f and g reads

$$f(z) = z\cosh(kz) - \frac{\sinh(kz)}{\tanh(k)}, \tag{A 9}$$

$$g(z) = -\frac{z^2}{4k}\sinh(kz) + \frac{\sinh(k) + 2k\cosh(k)}{4k^2\sinh(k)} z\cosh(kz) - \left[\frac{(1+Bi)(\cosh(k)(2k\coth(k)+1) - k\sinh(k)) + k^2\cosh(k)}{4k^2(k\cosh(k) + Bi\,\sinh(k))}\right]\sinh(kz). \tag{A 10}$$

The neutral stability relation (4.1) is obtained by inserting these expressions into the Marangoni boundary condition (A 3).

Appendix B. Perturbation method

In the perturbation procedure we consider the time-independent version of equations (2.13)–(2.17) with the pressure eliminated as in (3.1), (3.2). The mean flow U is assumed zero since the problem is translationally invariant with respect to the horizontal coordinate. The steady finite-amplitude solution is expanded in powers of a single, arbitrary perturbation parameter ϵ as

$$v_z = \epsilon v_z^{(1)} + \epsilon^2 v_z^{(2)} + \epsilon^3 v_z^{(3)} + \ldots, \tag{B 1}$$

$$\theta = \epsilon\theta^{(1)} + \epsilon^2\theta^{(2)} + \epsilon^3\theta^{(3)} + \ldots, \tag{B 2}$$

$$Ma = Ma^{(0)} + \epsilon Ma^{(1)} + \epsilon^2 Ma^{(2)} + \ldots. \tag{B 3}$$

From the expansion we obtain a set of equations at each order in ϵ. $Ma^{(n-1)}$ is determined by the solvability condition at order ϵ^n. Equation (B 3) defines the amplitude ϵ as function of the Marangoni number. At leading order we recover the neutral stability problem, giving $Ma^{(0)}$ as the critical Marangoni number and

$$v_z^{(1)}(x,z) = f^{(1)}(z)\cos(kx), \tag{B 4}$$

$$\theta^{(1)}(x,z) = g^{(1)}(z)\cos(kx), \tag{B 5}$$

with $f^{(1)}(z)$ and $g^{(1)}(z)$ given by (A 9) and (A 10). The solvability condition at second order gives $Ma^{(1)} = 0$. The second-order solution reads

$$v_z^{(2)}(x,z) = f^{(2)}(z)\cos(2kx), \tag{B 6}$$

$$\theta^{(2)}(x,z) = g_2^{(2)}(z)\cos(2kx) + Pg_0^{(2)}(z). \tag{B 7}$$

The functions $f^{(2)}(z)$, $g_2^{(2)}(z)$ are determined by the equations

$$\left(\mathrm{D}^2 - (2k)^2\right)^2 f^{(2)} = \left\{f^{(1)}\mathrm{D}^3 f^{(1)} - \mathrm{D}f^{(1)}\mathrm{D}^2 f^{(1)}\right\}, \tag{B 8}$$

$$\left(\mathrm{D}^2 - (2k)^2\right) g_2^{(2)} + f^{(2)} = \tfrac{1}{2}P\left\{f^{(1)}\mathrm{D}g^{(1)} - g^{(1)}\mathrm{D}f^{(1)}\right\}, \tag{B 9}$$

$$\mathrm{D}^2 f^{(2)}(1) + (2k)^2 Ma^{(0)} g_2^{(2)}(1) = 0, \tag{B 10}$$

$$\mathrm{D}^2 f^{(2)}(0) = f^{(2)}(0) = g_2^{(2)}(0) = 0, \tag{B 11}$$

$$f^{(2)}(1) = \mathrm{D}g_2^{(2)}(1) + Bi\, g_2^{(2)}(1) = 0, \tag{B 12}$$

and the x-independent temperature contribution $g_0^{(2)}(z)$ satisfies

$$\mathrm{D}^2 g_0^{(2)} = \tfrac{1}{2} P \mathrm{D}\left(g^{(1)} f^{(1)}\right), \tag{B 13}$$

$$g_0^{(2)}(0) = \mathrm{D}g_0^{(2)}(1) + Bi\, g_0^{(2)}(1) = 0. \tag{B 14}$$

The third-order solution again has a component with wavenumber k. It satisfies the system

$$(\mathrm{D}^2 - k^2)^2 f_1^{(3)} = \tfrac{1}{2}\left\{\mathrm{D}^2 f^{(2)} \mathrm{D} f^{(1)} - f^{(2)} \mathrm{D}^3 f^{(1)} - 3k^2 f^{(2)} \mathrm{D} f^{(1)}\right\} + \tfrac{1}{4}\left\{f^{(1)} \mathrm{D}^3 f^{(2)} - \mathrm{D}^2 f^{(1)} \mathrm{D} f^{(2)} - 3k^2 f^{(1)} \mathrm{D} f^{(2)}\right\}, \tag{B 15}$$

$$(\mathrm{D}^2 - k^2) g_1^{(3)} + f_1^{(3)} = \frac{P}{4}\left\{4 g_2^{(2)} \mathrm{D} f^{(1)} + 2 f^{(1)} \mathrm{D} g_2^{(2)} + 4 f^{(1)} \mathrm{D} g_0^{(2)} + g^{(1)} \mathrm{D} f^{(2)} + 2 f^{(2)} \mathrm{D} g^{(1)}\right\}, \tag{B 16}$$

$$\mathrm{D}^2 f_1^{(3)}(1) + k^2 Ma^{(0)} g_1^{(3)}(1) = -k^2 Ma^{(2)} g^{(1)}(1), \tag{B 17}$$

$$\mathrm{D}^2 f_1^{(3)}(0) = f_1^{(3)}(0) = g_1^{(3)}(0) = 0, \tag{B 18}$$

$$f_1^{(3)}(1) = \mathrm{D}g_1^{(3)}(1) + Bi\, g_1^{(3)}(1) = 0. \tag{B 19}$$

Equations (B 15)–(B 19) are an inhomogeneous version of the homogeneous neutral stability problem (A 1)–(A 5) with $\beta = 0$. The solvability condition determines the unknown coefficient $Ma^{(2)}$. With $Ma^{(2)} \neq 0$, the amplitude ϵ can be determined from the truncated Marangoni number expansion (B 3).

We have solved all of the equations (A 1)–(A 5), (B 8)–(B 12), (B 13)–(B 14), and (B 15)–(B 19) numerically using a finite difference scheme. To obtain the leading-order solution we prescribe the amplitude by replacing the Marangoni boundary condition with $g^{(1)}(1) = 1$. The inhomogeneous second-order problem can then be solved without modification since its homogeneous version will only have the trivial solution. At third order we must again replace the Marangoni boundary condition by $g_1^{(3)}(1) = 1$. $Ma^{(2)}$ is computed from the inhomogeneous Marangoni boundary condition (B 17) by inserting the solution of the modified third-order problem. Note that the solvability condition is not affected by the choice of the 'replacement' boundary condition.

REFERENCES

Ben Hadid, H. & Roux, B. 1992 Buoyancy- and thermocapillary-driven flows in differentially heated cavities for low-Prandtl-number fluids. *J. Fluid Mech.* **235**, 1–35.

Bestehorn, M. 1993 Phase and amplitude instabilities for Bénard–Marangoni convection in fluid layers with large aspect ratio. *Phys. Rev.* E **48**, 3622–3634.

Busse, F. H. & Clever, R. M. 1981 An aysmptotic model of two-dimensional convection in the limit of low Prandtl number. *J. Fluid Mech.* **102**, 75–83.

Canuto, C., Hussaini, M. Y., Quarteroni, A. & Zang, T. 1988 *Spectral Methods in Fluid Dynamics.* Springer.

Carpenter, B. M. & Homsy, G. M. 1990 High Marangoni number convection in a square cavity: Part II. *Phys. Fluids* A **2**, 137–149.

Chandrasekhar, S. 1961 *Hydrodynamic and Hydromagnetic Stability*. Oxford University Press.

Clever, R. M. & Busse, F. H. 1974 Transition to time-dependent convection. *J. Fluid Mech.* **65**, 625–645.

Clever, R. M. & Busse, F. H. 1981 Low-Prandtl-number convection in a layer heated from below. *J. Fluid Mech.* **102**, 61–74.

Clever, R. M. & Busse, F. H. 1990 Convection at very low Prandtl numbers. *Phys. Fluids* A **2**, 334–339.

Davidson, P. 1995 Magnetic damping of jets and vortices. *J. Fluid Mech.* **299**, 153–186.

Davis, S. H. 1987 Thermocapillary instabilities. *Ann. Rev. Fluid Mech.* **19**, 403–435.

Frisch, U. 1995 *Turbulence*. Cambridge University Press.

Ginde, R. M., Gill, W. N. & Verhoeven, J. D. 1989 An experimental study of Rayleigh–Bénard convection in liquid tin. *Chem. Engng Commun.* **82**, 223–228.

Gottlieb, D. & Orszag, S. A. 1977 *Numerical Analysis of Spectral Methods*. CBMS–NSF Regional Conference Series in Applied Mathematics, Philadelphia.

Jones, C. A., Moore, D. R. & Weiss, N. O. 1976 Axisymmetric convection in a cylinder. *J. Fluid Mech.* **73**, 353–388.

Kanouff, M. & Greif, R. 1994 Oscillations in thermocapillary convection in a square cavity. *Intl J. Heat Mass Transfer* **37**, 885–892.

Koschmieder, E. L. 1993 *Bénard Cells and Taylor Vortices*. Cambridge University Press.

Landau, L. D. & Lifshitz, E. M. 1987 *Fluid Mechanics*. Course of Theoretical Physics, vol. 6. Pergamon.

Levenstam, M. & Amberg, G. 1995 Hydrodynamical instabilities of thermocapillary flow in a half-zone. *J. Fluid Mech.* **297**, 357–372.

Longuet-Higgins, S. 1992 Capillary rollers and bores. *J. Fluid Mech.* **240**, 659–679.

Malkus, W. V. R. & Veronis, G. 1958 Finite amplitude cellular convection. *J. Fluid Mech.* **4**, 225–260.

Moore, D. R. & Weiss, N. O. 1973 Two-dimensional Rayleigh–Bénard convection. *J. Fluid Mech.* **58**, 289–312.

Moreau, R. 1990 *Magnetohydrodynamics*. Kluwer.

Nitschke, K., Bestehorn, M. & Thess, A. 1996 Square Cells in surface-tension-driven Bénard convection. submitted to *J. Fluid Mech.*

Nitschke, K. & Thess, A. 1995 Secondary instabilities in surface-tension-driven Bénard convection. *Phys. Rev.* E **52**, R5572–R5775.

Pearson, J. R. A. 1958 On convection cells induced by surface tension. *J. Fluid Mech.* **4**, 489–500.

Proctor, M. R. E. 1977 Inertial convection at low Prandtl number. *J. Fluid Mech.* **82**(1), 97–114.

Ruckenstein, E. 1968 Mass transfer in the case of interfacial turbulence induced by the Marangoni effect. *Intl. J. Heat Mass Transfer* **11**, 1753–1760.

Sarpkaya, T. 1996 Vorticity, free surface, and surfactants. *Ann. Rev. Fluid Mech.* **28**, 83–128.

Schatz, M. F., VanHook, S. J., McCormick, W. D., Swift, J. B. & Swinney, H. L. 1995 Onset of surface-tension-driven Bénard convection. *Phys. Rev. Lett.* **75**, 1938–1941

Slin'ko, M. G., Dil'man, V. V. & Rabinovich, L. M. 1983 Interfacial transfer in the presence of surface convective structures in liquid. *Theor. Found. Chem. Engng* **17**, 7–11.

Strani, M., Piva, R. & Graziani, G. 1983 Thermocapillary convection in a rectangular cavity: asymptotic theory and numerical simulation. *J. Fluid Mech.* **130**, 347–376.

Straughan, B. 1992 *The Energy Method, Stability, and Nonlinear Convection*. Springer.

Thess, A. & Orszag, S. A. 1995 Surface-tension-driven Bénard convection at infinite Prandtl number. *J. Fluid. Mech.* **283**, 201–230.

Thess, A., Spirn, D. & Jüttner, B. 1995 Viscous flow at infinite Marangoni number. *Phys. Rev. Lett.* **75**, 4614–4617.

Thual, O. 1992 Zero-Prandtl-number convection. *J. Fluid Mech.* **240**, 229–258.

VanHook, S. J., Schatz, M. F., McCormick, W. D., Swift, J. B. & Swinney, H. L. 1995 Long wavelength instability in surface-tension-driven Bénard convection. *Phys. Rev. Lett.* **75**, 4397–4400.

Veronis, G. 1966 Large-amplitude Bénard convection. *J. Fluid Mech.* **26**, 49–68.

Zebib, A., Homsy, G. M. & Meiburg, E. 1985 High Marangoni number convection in a square cavity. *Phys. Fluids* **28**, 3467–3476.